INFORMATICS JOURNALS
The Journal of Electrochemical Society of India, Volume 74, Issue (7&8), October – December 2025; pp. 228–246
ISSN (Print) : 0013-466X
ISSN (Online) : xxxx-xxxx
DOI: 10.18311/JESCI/2025/55212

Molecular Dynamics Study of Novel Sodium-lithium Electrolytes: $C_6H_3Na_3O_3$, $C_6H_3Na_2LiO_3$, $C_6H_3NaLi_2O_3$, and $C_6H_9Li_3O_3$

V. Annadurai[1], R Gopalkrishne[1] and R. Somashekar[2*]

[1]Department of Physics, NIE First Grade College, University of Mysore, Mysore - 570008, Karnataka, India

[2]Department of Studies in Physics, University of Mysore, Manasagangotri, Mysuru - 570006, Karnataka, India

Abstract

This paper presents a molecular dynamics study of four novel sodium-lithium electrolyte compounds: $C_6H_3Na_3O_3$, $C_6H_3Na_2LiO_3$, $C_6H_3NaLi_2O_3$, and $C_6H_9Li_3O_3$. These compounds, which have not been synthesised or reported in the literature, are explored as potential electrolytes for sodium- and lithium-ion batteries. Their structural stability, ionic behaviour, and transport properties are analysed to assess their suitability as next-generation energy storage materials.

Keywords: Battery Chemistry, Electrolyte Materials, Molecular Dynamics, Transport Properties, Sodium-ion Batteries

1. Introduction

The global pursuit of clean, renewable, and affordable energy sources has intensified research into sustainable energy storage technologies to mitigate environmental degradation and reduce dependence on fossil fuels[1]. Rechargeable batteries are central to this transition, underpinning advances in electric vehicles, grid-scale energy storage, and portable electronics. While Lithium-Ion Batteries (LIBs) dominate the market due to their high energy density and long cycle life, concerns related to the scarcity, uneven global distribution, high cost, and ethical issues associated with the mining of lithium and cobalt have prompted the search for alternative chemistries[2-5]. Challenges for rechargeable lithium batteries[6], issues and challenges facing rechargeable lithium batteries[7] and electrolytes and inter-phases in lithium-ion batteries and beyond[8,9].

Among emerging candidates, Sodium-based Batteries (SIBs) have garnered growing attention due to sodium's natural abundance, widespread availability, and lower cost. Sodium shares similar electrochemical behaviour with lithium, making it an attractive substitute for next-generation battery systems[4,10-13]. However, SIBs face challenges, including larger ionic radii, lower energy density, and difficulty achieving stable intercalation in common electrode materials. To overcome these limitations, recent studies have shifted focus towards Sodium metal anodes, which offer higher theoretical capacities (8~1166 $Ahkg^{-1}$) and improved voltage profiles[4,10,14-16].

One critical aspect influencing battery performance is the Solid Electrolyte Inter-phase (SEI) - a nanometric layer formed at the electrode-electrolyte interface that regulates ion transport, prevents dendrite formation, and stabilises cycling. In lithium and sodium metal batteries, a robust SEI is essential to suppress volumetric changes and parasitic reactions[17]. Consequently, material design for improved SEI compatibility remains a key area of interest.

Standard performance metrics include Columbic efficiency, defined as the ratio of discharge to charge capacity in a cycle:

$$\eta = \frac{C_d}{C_c} \times 100. \quad (1)$$

*Email: rs@physics.uni-mysore.ac.in

For stable lithium-ion systems, values typically range from 80% to 90%[18]. Specific capacity ($Ahkg^{-1}$), energy density ($Whkg^{-1}$), and power density (Wkg^{-1}) are additional critical figures of merit in evaluating battery efficiency. These depend on the nature of the active materials, electrolyte conductivity, and voltage windows. Exploring new electrolytes that support fast ion migration while ensuring electrochemical and mechanical stability is, therefore, central to battery innovation.

Recent reports have demonstrated the feasibility of sodium-metal pouch cells with tailored interphases, showing long cycle life and safety enhancements. For instance, Soni *et al.*[19] engineered multiphasic SEI layers to enable stable operation of Sodium-Sulfur (Na-S) batteries at room temperature, while Wang *et al.*[20] used fluorine-rich interfaces and sodiophilic frameworks to suppress dendrite growth and improve plating uniformity. Despite these promising results, practical application remains limited by interfacial in stability and low Columbic efficiency, emphasising the need for new materials with improved physical and electrochemical properties.

In this work, we address these challenges by designing and evaluating a new class of organo-metallic electrolytic materials composed of carbon, lithium, sodium, and oxygen. Specifically, we synthesised (*in silico*) four compounds: $C_6H_3Na_3O_3$, $C_6H_3Na_2LiO_3$, $C_6H_3NaLi_2O_3$, and $C_6H_9Li_3O_3$, and studied their thermo physical and battery-related properties using Molecular Dynamics (MD) simulations and shown in Figure 1. These compounds are inspired in part by the reported synthesis and structural characteristics of Li6O6 type organometallic systems[21], and aim to provide a pathway for multi-cationic, light-element-based materials with optimised transport and stability characteristics.

The molecular design of the proposed electrolytes was conceptually inspired by Li_6O_6-type organometallic clusters reported in the literature, in which a cyclic oxygen-rich coordination network stabilises multiple lithium ions. Following a similar structural rationale, we constructed a carbon-centred C_6 framework coordinated by three oxygen atoms, enabling stable binding of Na and Li in various stoichiometries. This analogy provides theoretical justification for the feasibility of multi-ion stabilisation and motivated the computational investigation of the new electrolyte candidates.

Structure notation and valency: Each C atom in the C_6 backbone is shown with hydrogens in Figure 1. The three

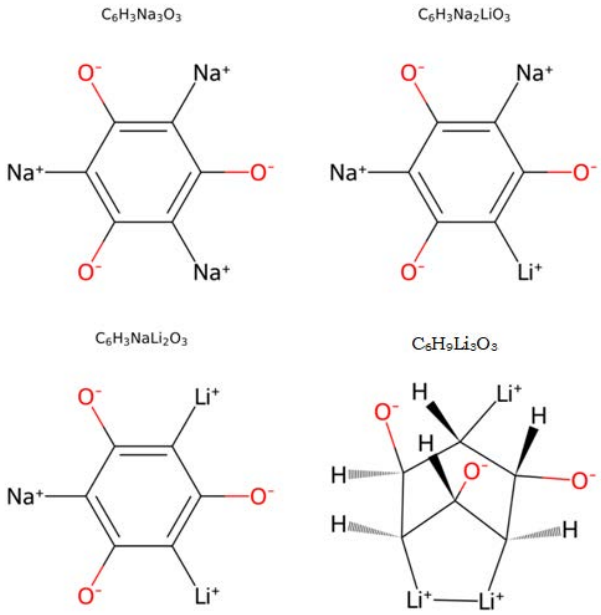


Figure 1. Chemical structure of four compounds: **(1)** $C_6H_3Na_3O_3$ **(2)** $C_6H_3Na_2LiO_3$ **(3)** $C_6H_3NaLi_2O_3$ **(4)** $C_6H_9Li_3O_3$.

oxygen atoms are represented as alkoxide centres ($C–O^-$); the negative charges on these oxygens are neutralised by the alkali cations (Li^+ and/or Na^+) so that each molecular formula shown ($C_6H_3Na_3O_3$, $C_6H_3Na_2LiO_3$, $C_6H_3NaLi_2O_3$, and $C_6H_9Li_3O_3$) is charge-balanced. For clarity, Figure 1 shows the H atoms and formal charges.

Our MD-based approach enabled the prediction of key material parameters, including density, specific heat, viscosity, ionic diffusivity, and dielectric behaviour. These were used to calculate derived battery metrics, such as Coulombic efficiency, energy density, and power density, under simulated cycling conditions. Additionally, we employed a *stochastic optimisation strategy* to identify the most promising candidate among the designed systems using a multi-parameter ranking.

2. Computational Methods

Since no experimentally determined crystal structure exists for $C_6H_3Na_3O_3$, $C_6H_3Na_2LiO_3$, $C_6H_3NaLi_2O_3$, and $C_6H_9Li_3O_3$, the initial condensed phases were generated using Packmol and optimised using DFT at the B3LYP/6-31G(d) level (LANL2DZ for Li/Na). Equilibration was performed in periodic simulation boxes under NPT conditions at 300 K and 1atm until structural convergence was achieved. The resulting structures represent stable, ionically bound solid phases, as confirmed by cohesive

energy and RDF analyses. No experimental crystal symmetry was assumed.

The initial design of the candidate electrolyte molecules was carried out using ChemDraw, from which SMILES (Simplified Molecular Input Line Entry System) strings were generated. These were subsequently converted to 3D molecular structures in Protein Data Bank (.pdb) format.

Refinement of molecular structures was performed using Visual Molecular

Dynamics (VMD)[22], where atom types, bond angles, and dihedrals were assigned using TkConsole commands such as topo retype bonds, topo guess angles, topo guess dihedrals and topo write lamps data. The resulting high-fidelity LAMMPS-compatible files were used for MD simulations. The simulation box for each electrolyte composition contained 200 molecules of $C_6H_3Na_3O_3$, $C_6H_3Na_2LiO_3$, $C_6H_3NaLi_2O_3$, and $C_6H_9Li_3O_3$, initially placed randomly in a cubic box (42×42×42 $Å^3$) using Packmol. Periodic boundary conditions were applied in all directions, and the systems were equilibrated via NPT ensemble at 300 K and 1atm until stable density and energy values were reached. The final equilibrated densities were found to be in the range of 1.42–1.58 gcm^{-3} depending on composition.

The Molecular dynamics simulations were performed using the OPLS-AA (Optimised Potentials for Liquid Simulations-All Atom) force field. OPLS-AA provides explicit representation of all atoms and has been extensively validated for ionic and electrolyte systems[23-25]. Standard parameters were used for C, H, and O atoms, while Li^+ and Na^+ ionic parameters were implemented from published electrolyte parameter sets.

Simulations were conducted using the Large-scale Atomic/Molecular Massively Parallel Simulator (LAMMPS)[23], employing the OPLS-AA force field[24-26] for atomistic parameterisation. All simulations were performed under three-dimensional periodic boundary conditions to represent an infinite bulk system. Long-range electrostatics were handled using the Particle Mesh Ewald (PME) method with a cutoff of 10Å. Periodicity was applied consistently during both NPT equilibration and NVT production runs to avoid finite-size and surface effects. All MD simulations were initially equilibrated in the NPT ensemble at 300K and 1atm to obtain the equilibrated densities and relaxed simulation cell dimensions. Temperature was controlled using the Nose-Hoover thermostat, and pressure control during NPT equilibration was implemented using the Parrinello-Rahman barostat. After equilibration, production simulations were carried out in the NVT ensemble at 300 K. These simulations enabled the calculation of a broad range of properties. A timestep of 1.0 fs was used for all molecular dynamics simulations.

The van der Waals interactions were treated using a Lennard-Jones potential with a cutoff of 12 Å, while electrostatic interactions were handled using the Particle-Particle Particle-Mesh (PPPM) Ewald method with a real-space cutoff of 12 Å and an accuracy of 10^{-4}. These details have now been clearly stated in the Computational Methods section to ensure reproducibility and transparency.

- *Structural and Thermodynamic*: Zero-point energy, entropy, density, specific gravity, thermal expansion coefficient. All mechanical, dielectric, phonon and thermodynamic properties were obtained using GULP. The GULP input contained the keywords "opti prop conp efg pot eem bond conq simu comp phon nofreq regi grad conv thermal", which enabled full geometry optimisation and automatic computation of zero-point energy, elastic constants, dielectric polarisation response, and phonon spectra. Phonon spectra were computed to analyse the system's vibrational properties. The calculations were performed using GULP 5.1 with the [specify potential, *e.g.*, Buckingham] potential. The optimised structure from energy minimisation was used as input, and the dynamical matrix was constructed using the phonon keyword in GULP. Eigen values of the dynamical matrix provided phonon frequencies throughout the Brillouin zone. Convergence criteria for geometry optimisation were set to [*e.g.*, 10^{-5} $eVÅ^{-1}$ for forces]. These phonon calculations are classical, based on a force-field model rather than full quantum-chemical DFT calculations. The resulting phonon spectra were analysed to confirm structural stability and extract the material's vibrational characteristics.
- Electric Field Gradient (EFG) at each atomic site was computed using GULP5.1. The optimised geometry of the system was obtained using the [specify potential, *e.g.*, Buckingham] potential with convergence criteria set to [*e.g.*, 10^{-5} $eVÅ^{-1}$ for forces]. The EFG keyword in GULP was employed to calculate the EFG tensors at all nuclei. For periodic systems, lattice summation was applied, and atomic charges were taken from

[charge model]. The computed EFG values were used to evaluate [properties, *e.g.*, quadrupolar coupling constants] and analyse the electronic environment at each atomic site.

- *Mechanical*: Elastic constants (C11, C12, C44, *etc.*), Young's, shear and bulk moduli, linear compressibility, Poisson's ratio, spatial variation of these parameters.
- *Dielectric and Optical*: Dielectric constants, refractive index, Bruggeman coefficient.
- *Transport*: Diffusivity, viscosity, surface tension, thermal conductivity.
- *Electrochemical*: Columbic efficiency, specific capacity, energy and power densities, voltage-time and voltage-capacity profiles.

To evaluate electrochemical performance in battery applications, we used the Python Battery Mathematical Modelling (PyBaMM) framework[27], which supports detailed simulations of lithium-ion systems. PyBaMM allowed us to assess charge/discharge behaviour, capacity retention, Columbic efficiency, thermal effects, and degradation mechanisms across both standard and novel electrolytes. In addition, accustom Python program was written to compute specific capacity, energy density, and power density. Static lattice properties such as lattice energy and elastic moduli were evaluated using GULP (General Utility Lattice Program)[28], based on classical force fields.

UV-Vis, Infrared (IR) and NMR spectra were computed using the WebMO online program[29]. IR, UV-Visible and NMR spectra were computed separately using WebMO. The WebMO calculations used the levels of theory HF/3-21G Freq PM6 with VSTO-6G basis and HV method for all compounds. These spectral results were obtained after structural optimisation and frequency confirmation. All quantum chemical calculations were performed using the WebMO interface, employing its underlying quantum chemistry engines. Geometry optimisations were carried out until the maximum force on atoms was less than 10^{-4} a.u., ensuring well-converged optimised structures. All spectroscopic results (UV-Vis, IR, and NMR) presented in this study are purely computational. No experimental synthesis or experimental spectra were used or compared. Geometry optimisations and IR calculations were performed using HF/3-21G, while UV-Vis spectra were obtained using TD-DFT at the same optimised geometry, and NMR calculations were performed using PBE/STO-3G.

3. Results and Discussion

3.1 Comparative Analysis of Thermodynamic and Structural Properties

A comparative evaluation of the four electrolyte compounds: $C_6H_3Na_3O_3$, $C_6H_3Na_2LiO_3$, $C_6H_3NaLi_2O_3$, and $C_6H_9Li_3O_3$ reveals important insights into their thermodynamic stability, electronic behaviour, and structural properties. The nature and proportion of alkali metal constituents (Na and Li) significantly influence their characteristics.

Among the four, $C_6H_9Li_3O_3$ exhibits the highest thermodynamic stability, as indicated by its most negative self-energy (-1.49 eV) and Helmholtz free energy (-11.25 eV). It also demonstrates the highest entropy value (0.0419, $Jmol^{-1}K^{-1}$), suggesting greater structural flexibility or molecular disorder. Its specific gravity (177.04) is the highest among the samples, confirming a dense packing. However, its electrical conductivity is the lowest (9.76e-24 Sm^{-1}), indicating poor charge transport, which may limit its practical application in fast-ion conducting environments.

In contrast, $C_6H_3NaLi_2O_3$ presents a more balanced profile. It shows the highest electrical conductivity (1.14e-20 Sm^{-1}) among all compounds, which can be attributed to a synergistic effect between Na^+ and Li^+ ions that likely enhances ionic mobility. Its thermodynamic parameters, such as self-energy (-0.37 eV) and Helmholtz free energy (-2.55 eV), are moderate, indicating sufficient stability for practical use.

$C_6H_3Na_2LiO_3$ displays the highest density (0.0110 gcm^{-3}) and zero-point energy (0.2388 eV), indicating a tightly packed yet vibrationally active structure. However, its entropy is the lowest (0.0034 $Jmol^{-1}K^{-1}$), suggesting limited structural flexibility.

The sodium-rich compound $C_6H_3Na_3O_3$ is comparatively less favourable. It has the least negative self-energy (-0.37 eV), moderate density, and a relatively low specific gravity (131.95). Its electrical conductivity (2.22e-20 Sm^{-1}) is higher than that of $C_6H_9Li_3O_3$ but remains insufficient for optimal electrolyte performance.

3.2 Comparative Analysis of Thermodynamic, Structural, and Transport Properties

A comparative assessment of the four electrolyte compositions- $C_6H_3Na_3O_3$, $C_6H_3Na_2LiO_3$, $C_6H_3NaLi_2O_3$,

Table 1. Thermodynamic and structural properties

Property	$C_6H_3Na_3O_3$	$C_6H_3Na_2LiO_3$	$C_6H_3NaLi_2O_3$	$C_6H_9Li_3O_3$
Electro negativity (eV)	6.47	6.54	6.47	6.55
Self-energy (eV)	-0.37	-0.15	-0.37	-1.49
Zero-point Energy (eV)	0.0096	0.2388	0.0155	0.0628
Entropy ($Jmol^{-1}K^{-1}$)	0.0091	0.0034	0.0092	0.0419
Helmholtz free energy (eV)	-2.52	-2.69	-2.55	-11.25
Density(gcm^{-3})	0.054	0.0110	0.0031	0.0081
Specific Gravity	131.95	144.19	158.94	177.04
Electrical conductivity (Sm^{-1})	2.22e-20	2.21e-23	1.14e-20	9.76e-24

Table 2. Mechanical properties

Property	$C_6H_3Na_3O_3$	$C_6H_3Na_2LiO_3$	$C_6H_3NaLi_2O_3$	$C_6H_9Li_3O_3$
Young's Modulus (GPa)	0.011	3.815	3.815	0.012
Shear Modulus (GPa)	0.004	3.095	3.095	0.005
Bulk Modulus (GPa)	0.055	0.719	0.719	0.008
Poisson's Ratio	0.465	-0.384	-0.384	0.244

and $C_6H_9Li_3O_3$ provides insights into how alkali-metal substitution governs thermodynamic stability, electronic transport, and mechanical response. The relative proportions of Na^+ and Li^+ strongly influence the energetic landscape and structure–property relationships (Table 1).

Among the four systems, $C_6H_9Li_3O_3$ exhibits the highest thermodynamic stability, as evidenced by its most negative self-energy (−1.49 eV) and Helmholtz free energy (−11.25 eV). This compound also shows the highest entropy (0.0419 $Jmol^{-1}K^{-1}$), suggesting enhanced structural flexibility or configurational disorder. Its high specific gravity (177.04) indicates dense atomic packing. However, this structural compactness coincides with extremely low electrical conductivity ($9.76 \times 10^{-24}\ Sm^{-1}$), implying limited charge transport and reduced suitability for fast-ion-conducting electrolyte environments.

In contrast, $C_6H_3NaLi_2O_3$ demonstrates a more balanced performance profile. It exhibits the highest electrical conductivity among the compounds studied (1.14 × 10−20 Sm−1), attributable to synergistic interactions between Na+ and Li+ ions that enhance ionic mobility. Its intermediate self-energy (−0.37 eV) and Helmholtz free energy (−2.55 eV) indicate sufficient thermodynamic stability while maintaining favorable transport properties.

The compound $C_6H_3Na_2LiO_3$ exhibits the highest mass density (0.0110 g cm^{-3}) and zero-point energy (0.2388 eV), indicating a tightly packed yet vibrationally active lattice. However, its low entropy value (0.0034 $Jmol^{-1}K^{-1}$) suggests limited configurational freedom, which may restrict long-range ion transport.

The sodium-rich system $C_6H_3Na_3O_3$ is comparatively less favourable. It exhibits the lowest negative self-energy (−0.37 eV), a moderate density, and a lower specific gravity (131.95). While its electrical conductivity (2.22× 10−20 Sm^{-1}) exceeds that of $C_6H_9Li_3O_3$, it remains insufficient for high-performance electrolyte applications.

3.3 Mechanical Stability and Lattice Response

Commercial liquid electrolytes typically possess negligible mechanical stiffness (shear modulus 0.01 GPa). In contrast, $C_6H_3Na_2LiO_3$ and $C_6H_3NaLi_2O_3$ exhibit solid-like mechanical stability (Table 2), making them attractive candidates for solid-state battery architectures. The enhanced shear modulus observed in mixed Na-Li systems is particularly relevant for suppressing dendrite penetration, a major failure mechanism in metal-based batteries.

FThe spatial variation in elastic constants and Poisson's ratio among the four compounds (Figure 2) can be rationalised by differences in electronic orbital distributions and atomic configurations. Sodium and lithium rich systems tend to exhibit more delocalized

electronic clouds, whereas mixed Na-Li compositions promote more directional bonding, likely involving p- and d- orbital contributions. This transition toward directional bonding enhances rigidity while reducing ductility, consistent with the observed mechanical trends.

Negative Poisson's ratios, observed in certain cases, may indicate auxetic or metastable mechanical behaviour

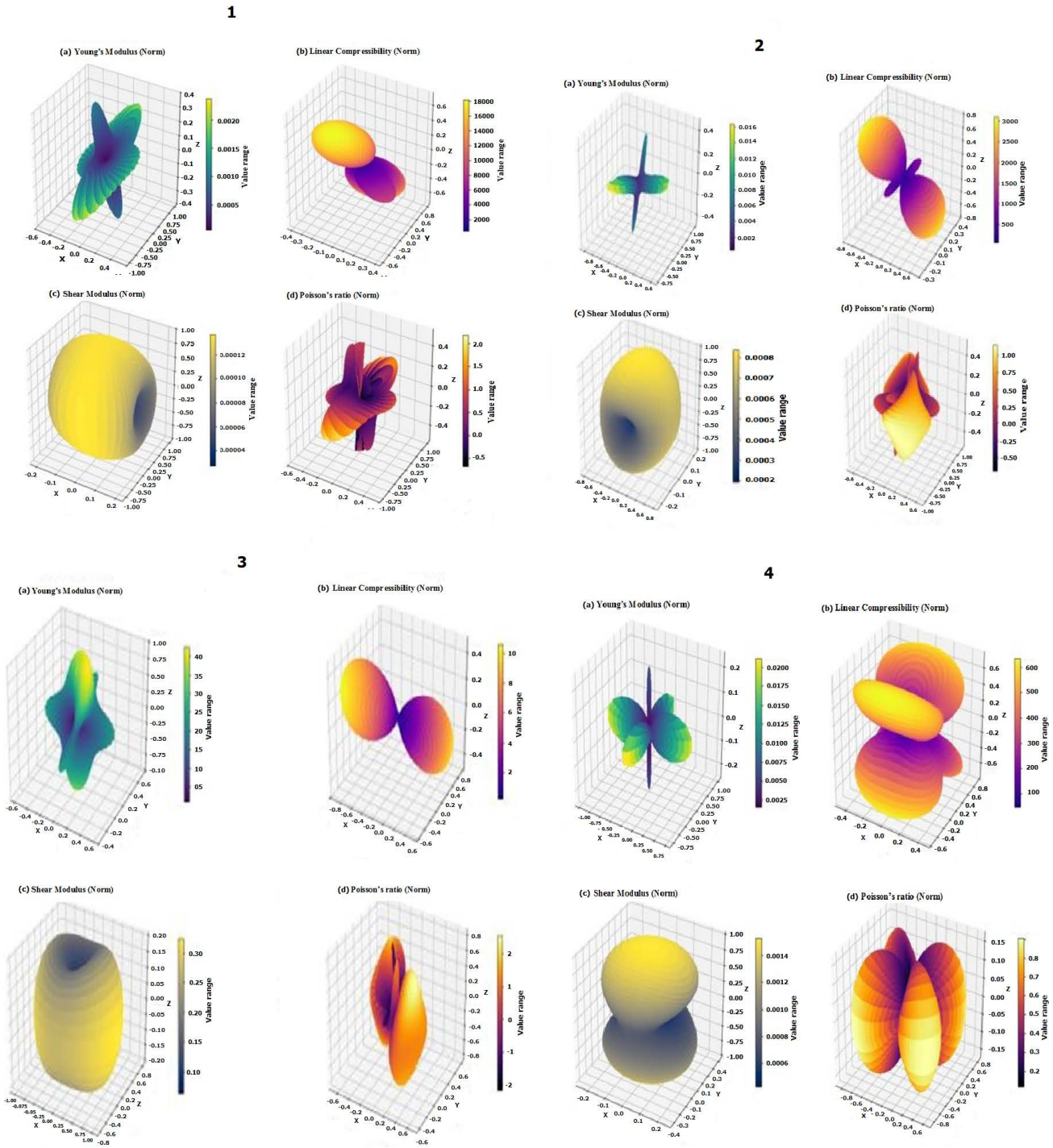


Figure 2. Spatial variation of **(a)** Young's modulus, **(b)** Linear compressibility, **(c)** Shear modulus, and **(d)** Poisson's ratio of four compounds: **(1)** $C_6H_3Na_3O_3$, **(2)** $C_6H_3NaLi_2O_3$, **(3)** $C_6H_3Na_2LiO_3$, and **(4)** $C_6H_9Li_3O_3$.

and warrant further investigation to assess long-term structural stability under electrochemical cycling.

3.4 Dielectric, Phonon and Electric Field Gradient Analysis

Among the studied compounds, $C_6H_3Na_3O_3$ exhibits the highest dielectric constant and refractive index, reflecting enhanced polarisability (Figure 3). In contrast, $C_6H_3Na_2LiO_3$ shows pronounced phonon Density of States (DOS) peaks, indicative of strong vibrational activity and lattice rigidity. $C_6H_3NaLi_2O_3$ and $C_6H_9Li_3O_3$ display intermediate dielectric and optical behaviour.

Electric Field Gradient (EFG) analysis (Figure 4) reveals that $C_6H_3Na_3O_3$ possesses the most uniform local electric environment, whereas $C_6H_3Na_2LiO_3$ exhibits significant EFG distortion. This distortion may enhance ion mobility but could also introduce field-induced instabilities. Overall, all four systems exhibit lower dielectric constants than conventional liquid electrolytes, reinforcing their suitability primarily for solid-state battery configurations.

3.5 Spectroscopic Signatures

The UV-Vis (Ultraviolet-Visible) spectra (Figure 5a) reveal progressive sharpening and spectral shifts with increasing lithium content, indicating enhanced electron localisation. Infrared spectra (Figure 5b) show increasingly well-defined vibrational peaks with Li substitution, consistent with reduced atomic mass and stronger bond force constants. NMR (Nuclear Magnetic

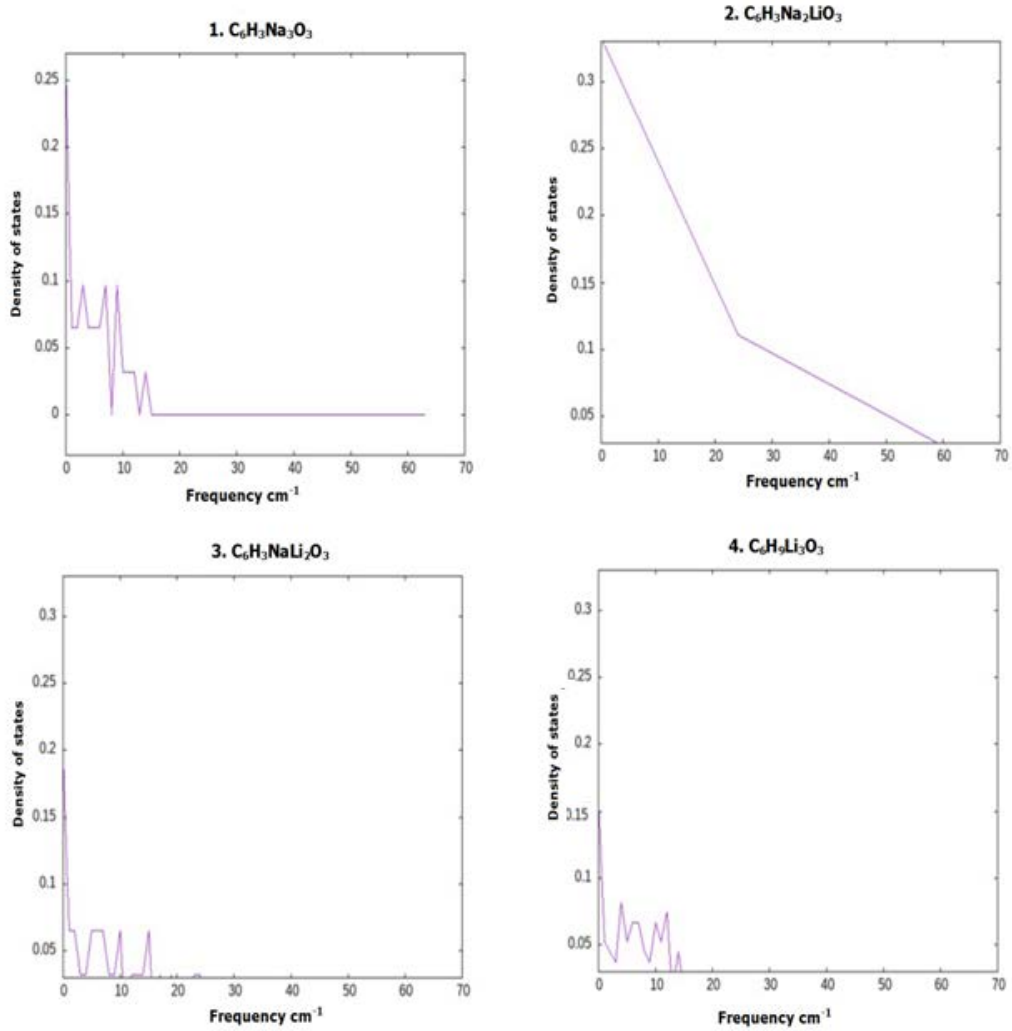


Figure 3. Density of States (DOS) from phonon absorption spectra of four compounds: **(1)** $C_6H_3Na_3O_3$, **(2)** $C_6H_3Na_2Li_2O_3$, **(3)** $C_6H_3NaLiO_3$, and **(4)** $C_6H_9Li_3O_3$.

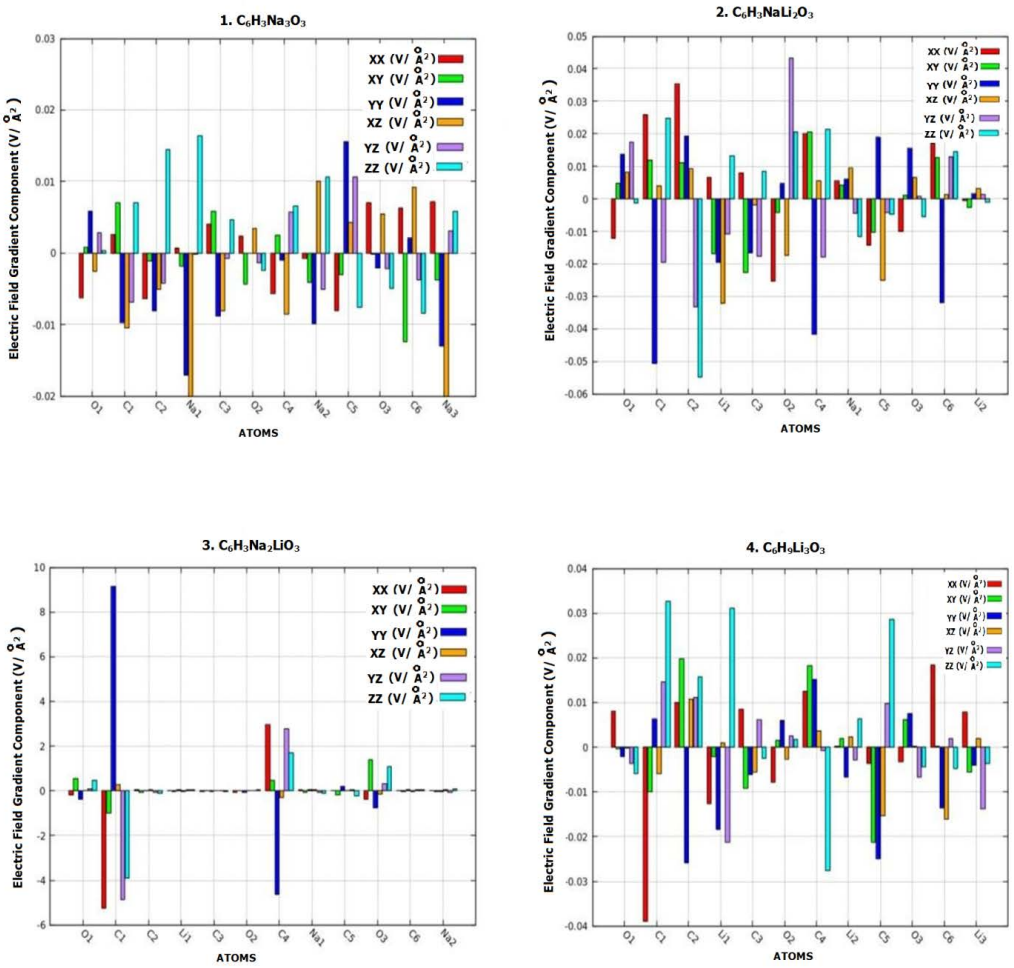


Figure 4. Electric field gradient of four compounds: **(1)** $C_6H_3Na_3O_3$, **(2)** $C_6H_3NaLi_2O_3$, **(3)** $C_6H_3Na_2LiO_3$, and **(4)** $C_6H_9Li_3O_3$.

Resonance) chemical shifts (Figure 5c) exhibit increased dispersion with lithium content, reflecting pronounced changes in the local electronic environment surrounding carbon atoms.

3.6 Transport Properties and Electrochemical Performance

Among the four systems, $C_6H_3NaLi_2O_3$ stands out in terms of ionic diffusivity, approaching values characteristic of standard Li^+ electrolytes. Its low viscosity and surface tension favour efficient ion transport and interfacial wetting, while its thermal conductivity surpasses that of the other candidates (Table 4; Figures 6, 7). $C_6H_3Na_2LiO_3$ also demonstrates moderate diffusivity and favourable thermal behaviour.

Battery-level simulations indicate that $C_6H_9Li_3O_3$ delivers the most stable electrochemical performance, closely resembling conventional Li^+ electrolytes in terms of voltage stability, capacity retention, and current response (Table 5; Figure 8). $C_6H_3Na_2LiO_3$ exhibits intermediate performance, outperforming purely sodium-based systems, whereas $C_6H_3Na_3O_3$ and $C_6H_3NaLi_2O_3$ underperform due to limited ionic mobility or stability constraints.

3.7 Electrochemical Performance Metrics

Electrochemical metrics were computed using the Doyle-Fuller-Newman (DFN) model implemented in PyBaMM. Coulombic efficiency, specific capacity, energy density, power density, and charge-discharge intersection voltage were evaluated by numerically integrating current-voltage profiles (Figure 9). The adopted methodology ensures consistency and comparability across all electrolyte systems.

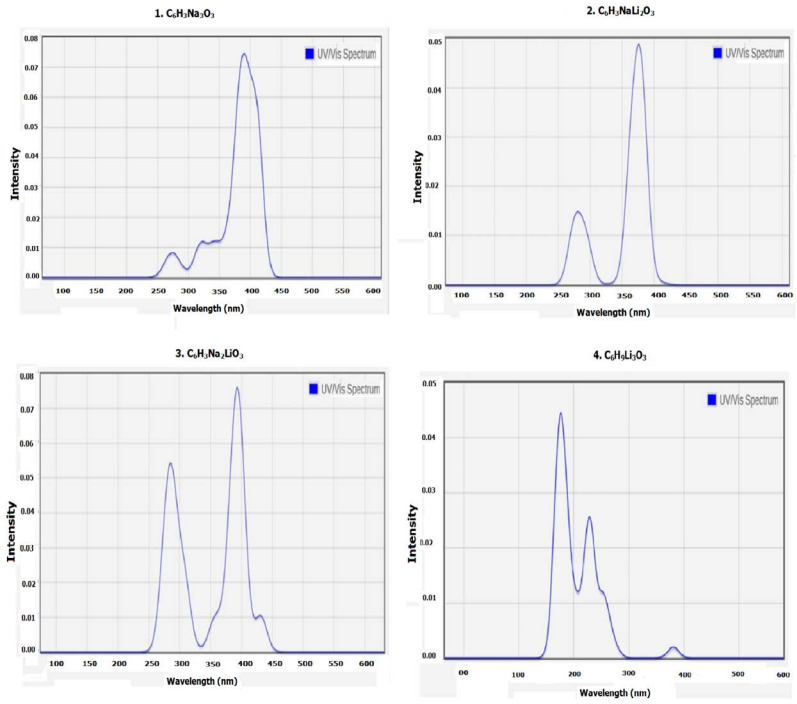


Figure 5(a). UV-Vis spectra of four compounds: **(1)** $C_6H_3Na_3O_3$ **(2)** $C_6H_3NaLi_2O_3$ **(3)** $C_6H_3Na_2LiO_3$ **(4)** $C_6H_9Li_3O_3$.

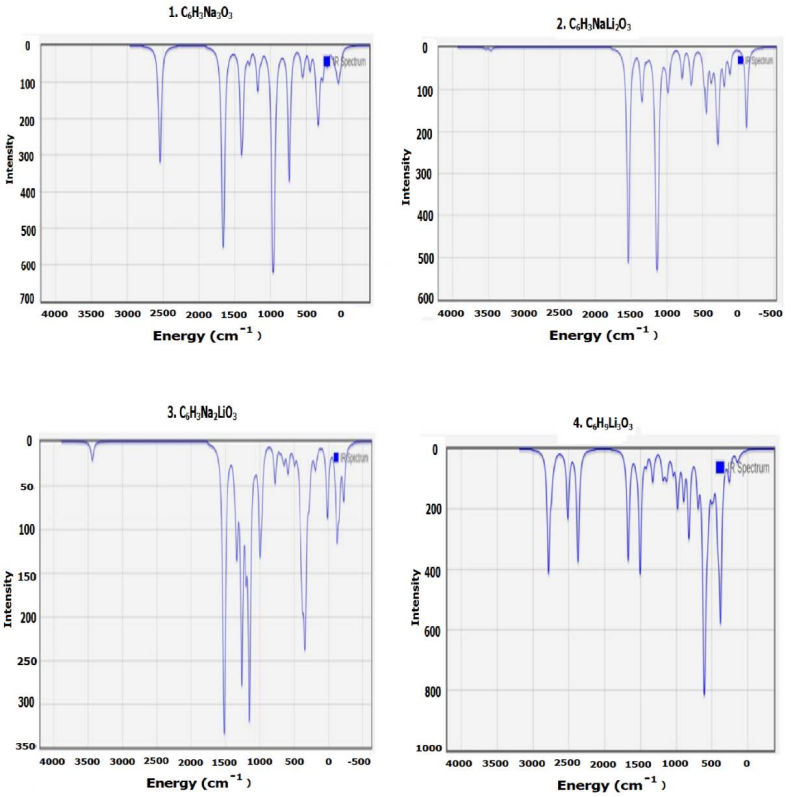


Figure 5(b). IR Spectra of four compounds: **(1)** $C_6H_3Na_3O_3$ **(2)** $C_6H_3NaLi_2O_3$ **(3)** $C_6H_3Na_2LiO_3$ **(4)** $C_6H_9Li_3O_3$.

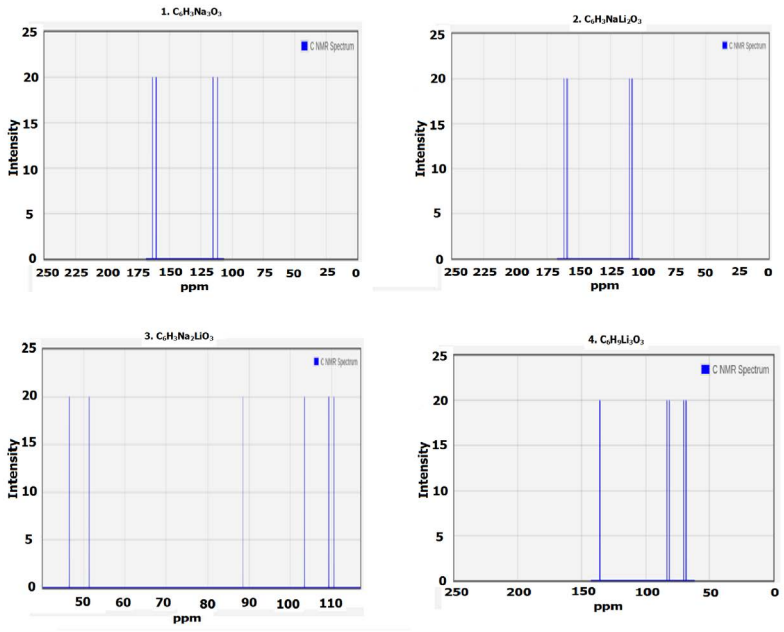


Figure 5(c). NMR spectra of four compounds: **(1)** $C_6H_3Na_3O_3$ **(2)** $C_6H_3NaLi_2O_3$ **(3)** $C_6H_3Na_2LiO_3$ **(4)** $C_6H_9Li_3O_3$.

Table 4. Transport properties

Property	$C_6H_3Na_3O_3$	$C_6H_3Na_2LiO_3$	$C_6H_3NaLi_2O_3$	$C_6H_9Li_3O_3$
Ionic Diffusivity (cm^2s^{-1})	1.20e-14	4.94e-14	9.19e-8	9.19e-14
Viscosity (Pa.s)	4.45e-10	9.19e-9	1.54e-10	4.45e-10
Surface Tension (mNm^{-1})	0.0010	0.0029	0.0004	0.0041
Thermal Conductivity ($Wm^{-1}K^{-1}$)	5.87e-07	4.655e-5	3.30e-5	2.17e-6

(i) Columbic Efficiency (ηC)

Columbic efficiency quantifies the reversibility of the electrochemical reactions during a charge-discharge cycle. It is defined as the ratio of the discharge capacity to the charge capacity: $\eta_C = \frac{Q_{Discharge}}{Q_{Charge}} \times 100$. Where Qdischarge is the total capacity during discharge (in Ah), Qcharge is the total capacity during charging (in Ah) (Figure 9). Both capacities were calculated using numerical integration over current:

$$Q = \frac{1}{3600}\int_{t_0}^{t_f} I(t).dt \qquad (2)$$

The integral was evaluated using the trapezoidal rule on current-versus-time data. I(t)>0 during discharge and $I(t)$<0 during charge. If only discharge is simulated (as in single-cycle cases), then Qcharge = 0, and the columbic efficiency cannot be computed meaningfully.

(ii) Specific Capacity (Ccp)

Specific capacity represents the amount of electric charge extracted per unit mass of the battery and is a key performance metric for energy storage materials. $C_{cp} = \frac{Q_{charge}}{m}$. Assuming a unit battery mass (1kg) for comparative modelling purposes, we have Ccp= Qcharge [Ah kg-1].

(iii) Energy Density (Eden)

Energy density quantifies the total energy extracted per unit mass during discharge: $E_{den} = \frac{1}{3600}\int_{t_0}^{t_f} V(t).I(t).dt$ where V(t) is the terminal voltage, I(t) is the discharge current, and the factor (1/3600) converts the result from watt-seconds (Joules) to Watt-hours (Wh). This metric provides insight into how much usable energy the battery delivers.

(iv) Power Density (Pden)

Power density is defined as the rate of energy delivery per unit mass: $P_{den} = \frac{E_{den}}{t_{discharge}}$, where Eden is the energy density

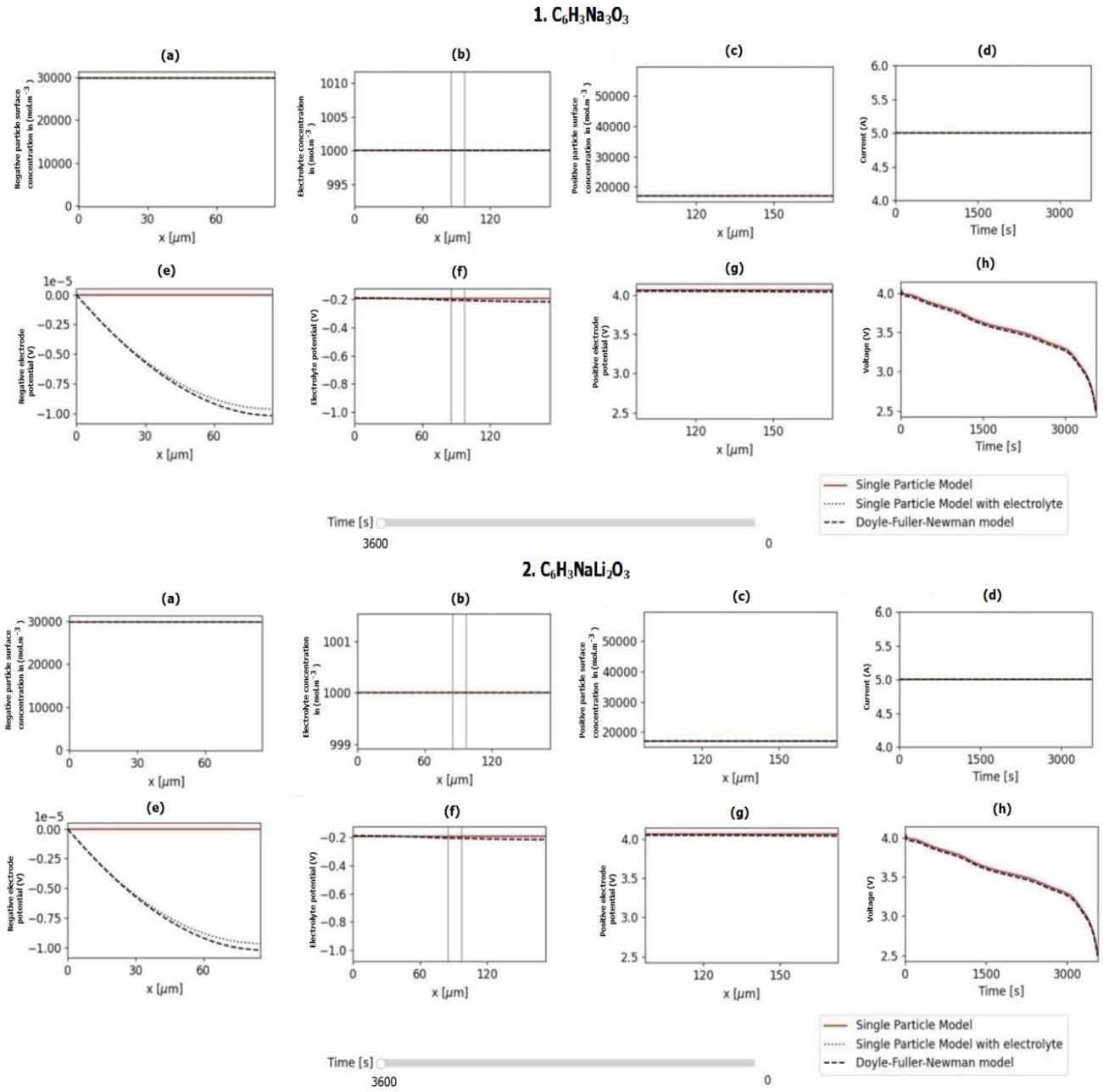


Figure 6. Battery properties compared with a standard lithium battery. **1(a-h):** $C_6H_3Na_3O_3$, and **2(a-h):** $C_6H_3NaLi_2O_3$.

(Whkg^{-1}), and tdischarge is the total discharge duration (in hours).

(v) Voltage at Intersection of Charge and Discharge Curves (Vint)

The voltage intersection represents the average voltage at which the charging and discharging voltage curves overlap or approach each other most closely. It is estimated by aligning the voltage curves during discharge and charge cycles and computing the mean of the corresponding voltage values: $V_{\text{int}} = \frac{1}{n}\sum_{i=1}^{n} \frac{V_{dis}(i)+V_{ch}(i)}{2}$, where $V_{dis}(i)$ and $V_{ch}(i)$ are the voltages at the same relative time point in discharge and charge. n is the minimum of the two curve lengths, and it provides a representative midpoint voltage between charge and discharge behaviour.

Figures 6 and 7 show battery properties compared with a standard lithium battery for all four electrolytes. Figure 8 indicates the variation in Voltage, Current, and Capacity of the four compounds, and Figure 9 shows

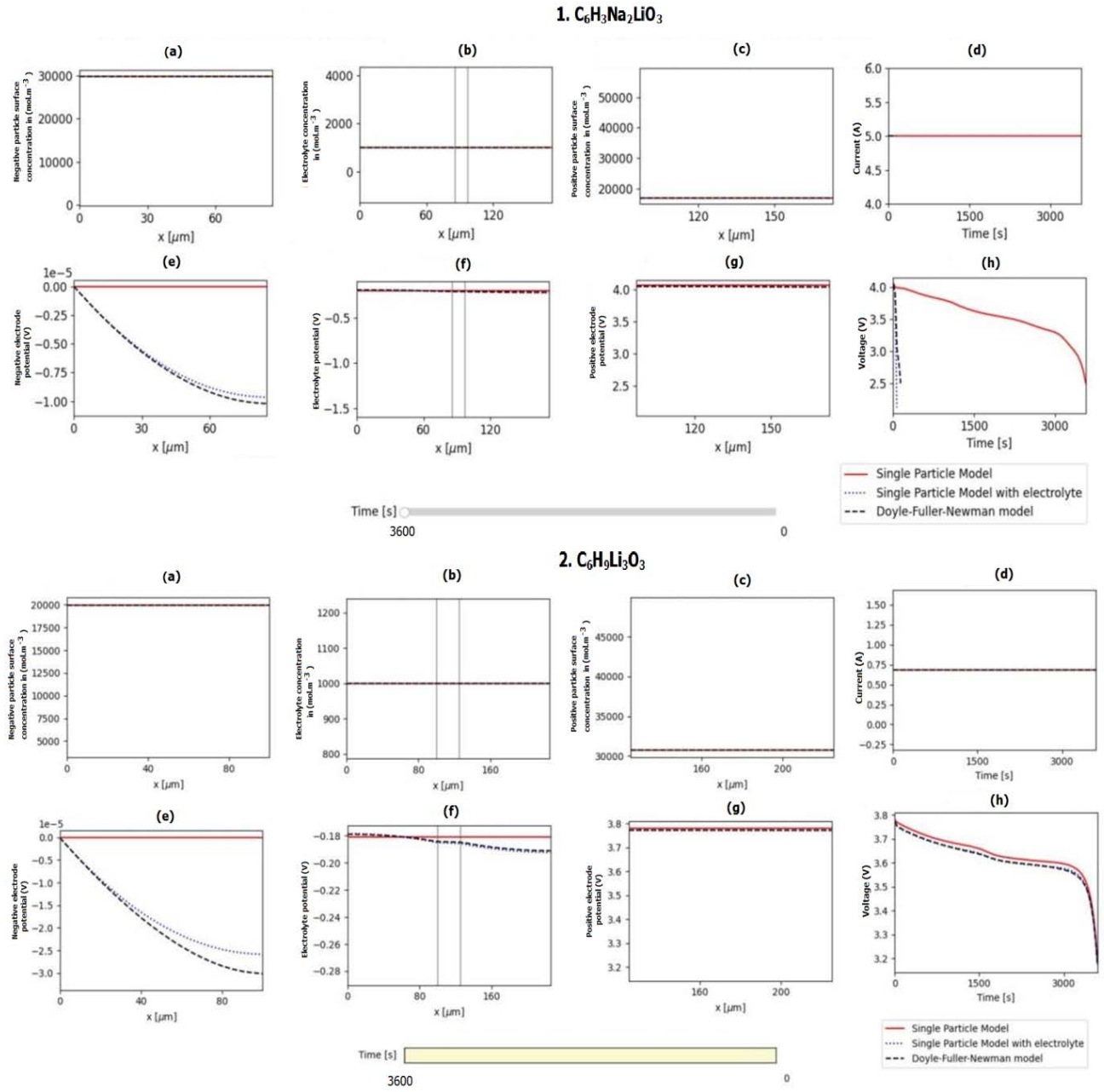


Figure 7. Battery properties in comparison with standard lithium battery: **(1)** $C_6H_3Na_2LiO_3$ and **(2)** $C_6H_9Li_3O_3$.

Table 5. Battery performance metrics (from PyBaMM)

Metric	$C_6H_3Na_3O_3$	$C_6H_3Na_2LiO_3$	$C_6H_3NaLi_2O_3$	$C_6H_9Li_3O_3$
Coulomb Efficiency (%):	0.0	211.3	171.4	237.4
Specific Capacity (Ahg^{-1})	0.222	0.186	1.250	0.175
Voltage at Intersection (V)	0.0	3.69	4.08	3.79
Energy Density (Whkg^{-1})	0.746	0.644	4.958	0.712
Power Density (Wkg^{-1})	8.411	8.663	9.916	8.760
Dipolemoment (Debye)	2.58	2.73	1.62	6.53

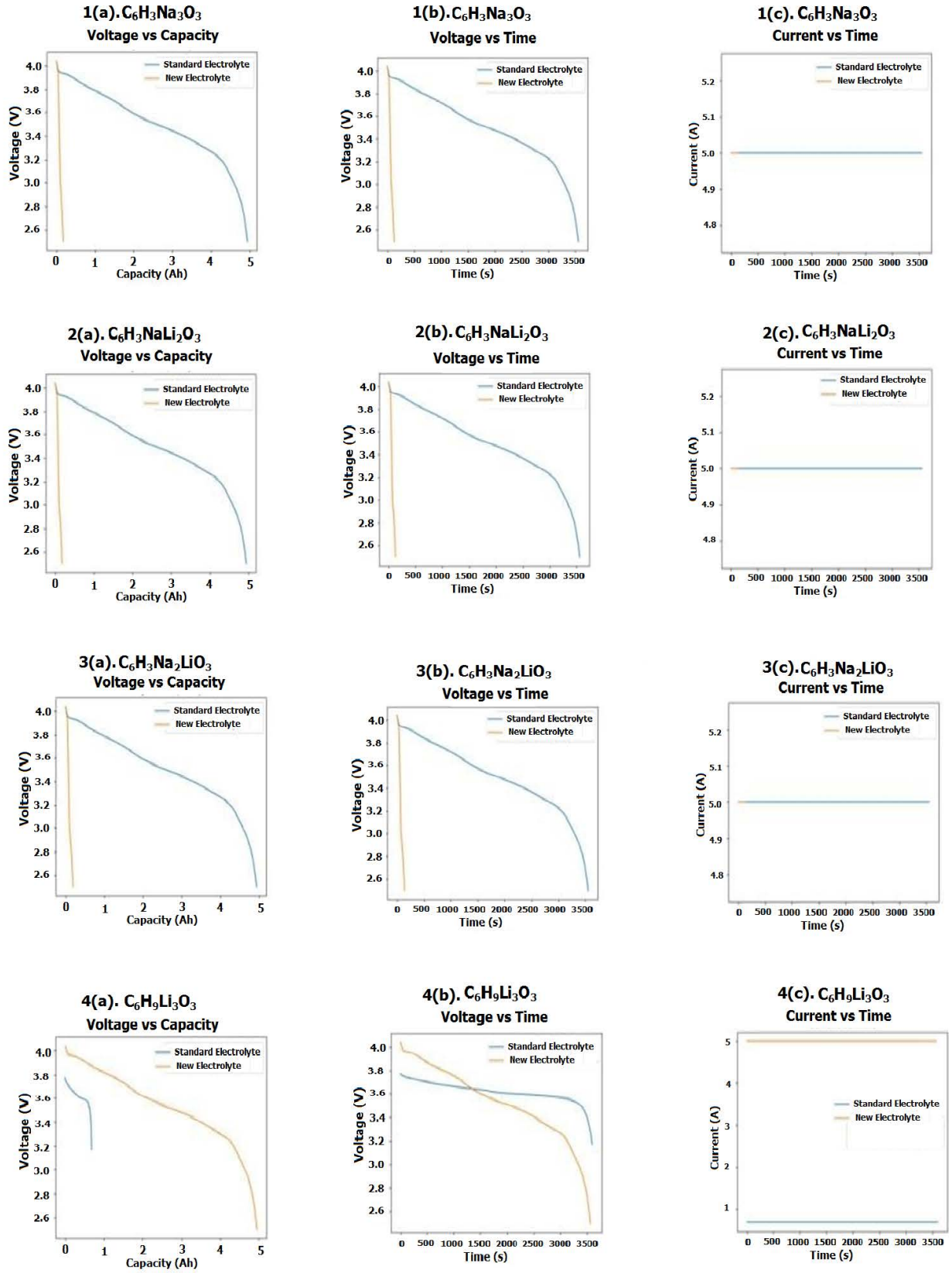


Figure 8. Variation of **(a)** Voltage *vs* Capacity **(b)** Voltage *vs* Time **(c)** Current *vs* Time of four compounds: **1(a-c)** $C_6H_3Na_3O_3$ **2(a-c)** $C_6H_3NaLi_2O_3$ **3(a-c)** $C_6H_3Na_2LiO_3$ **4(a-c)** $C_6H_9Li_3O_3$.

Table 3. Vibrational, optical, and electrical properties

Property	$C_6H_3Na_3O_3$	$C_6H_3Na_2LiO_3$	$C_6H_3NaLi_2O_3$	$C_6H_9Li_3O_3$
Phonon DOS Peaks (cm^{-1})	3.0;7.0;9.0	24.0;96.0	7.0;10.0;15.0	4.0;6.0:7.0:10.0:12.0
Refractive Index	1.40	1.20	1.11	1.29
Dielectric Constant	3.7	1.36	1.23	1.54
Bruggeman Coefficient	0.215	0.215	0.215	0.215

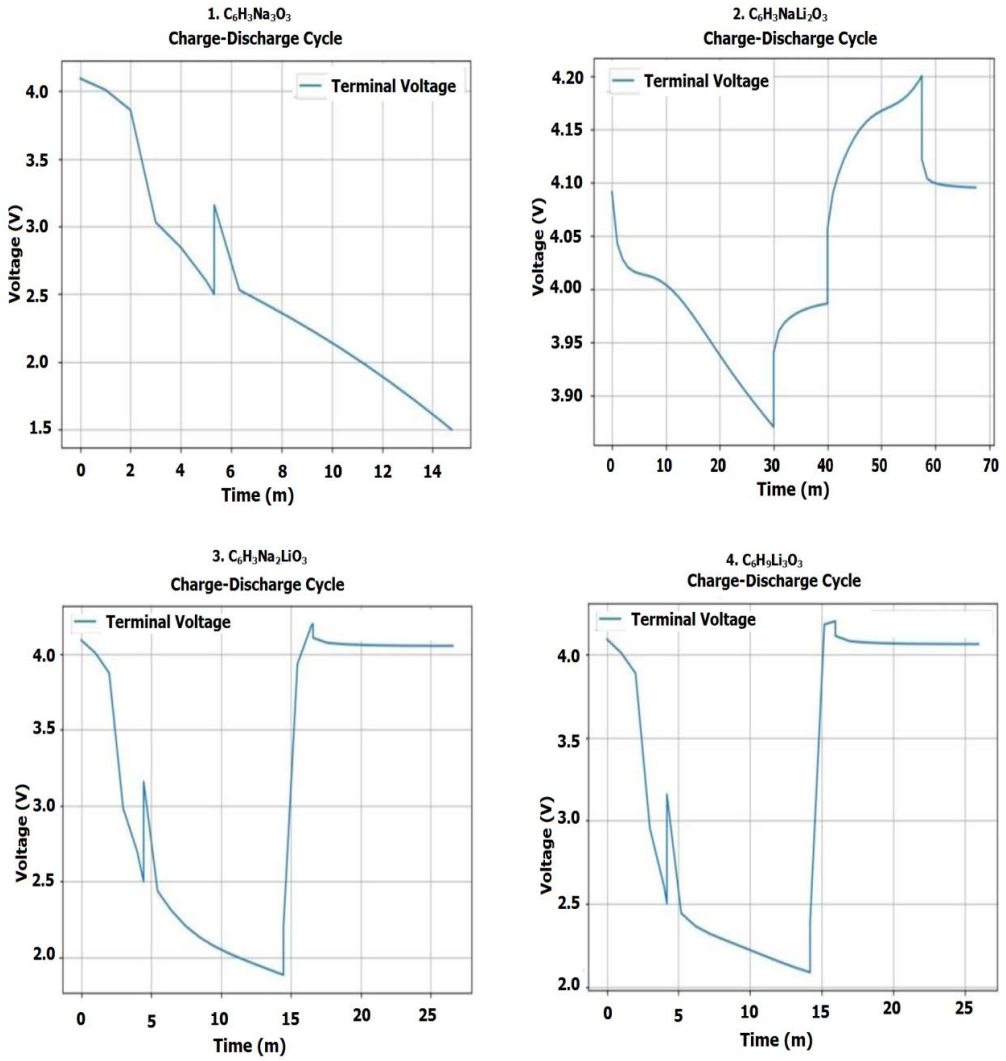


Figure 9. Charging and discharging of voltage versus time of four compounds: **(1)** $C_6H_3Na_3O_3$, **(2)** $C_6H_3NaLi_2O_3$, **(3)** $C_6H_3Na_2LiO_3$, and **(4)** $C_6H_9Li_3O_3$.

the charging and discharging of Voltage for the four compounds.

3.8 Stochastic Analysis of Battery Parameters

To quantify the effect of $Na^+ \rightarrow Li^+$ substitution, battery performance parameters were treated as realizations of a continuous stochastic process with measurement uncertainty. Functional Principal Component Analysis (FPCA) was applied to extract dominant modes of variation and correlation structures across compositional space (Figure 10). The analysis reveals systematic trends, showing that increasing Li^+ content enhances ionic

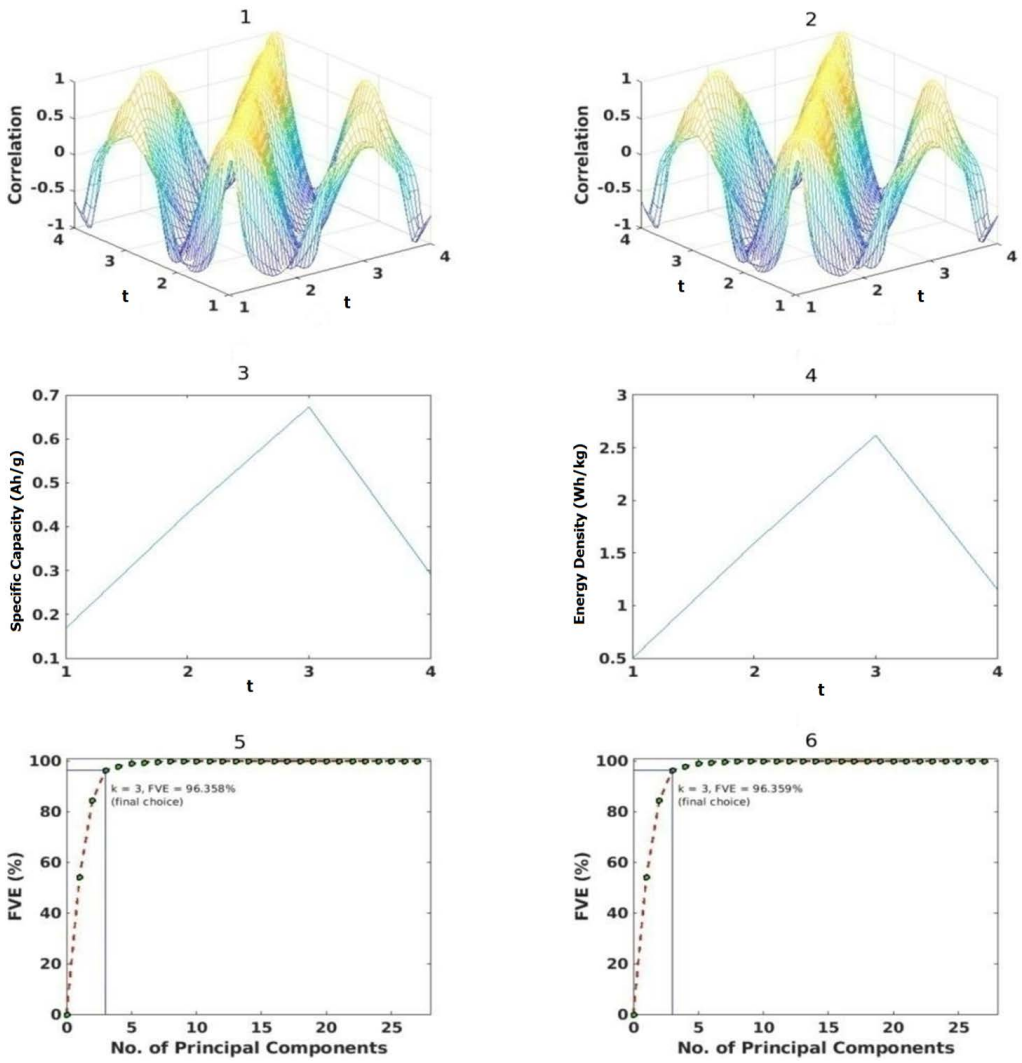


Figure 10. 1st row Surface correlation, 2nd row Mean value (Number 3 is for Specific capacity (Ah/g) *vs* t, Number 4 is for Energy density (Wh/kg) *vs* t), 3rd row Principal components for continuous increase in Li^+. 't' values in the graphs correspond to **(1)** $C_6H_3Na_3O_3$ **(2)** $C_6H_3Na_2LiO_3$ **(3)** $C_6H_3NaLi_2O_3$ **(4)** $C_6H_9Li_3O_3$.

transport and electrochemical stability, consistent with prior studies on mixed-alkali electrolytes. FPCA further identifies parameters most sensitive to compositional tuning, providing a quantitative basis for rational electrolyte design.

4. Conclusion

- $C_6H_9Li_3O_3$ is thermodynamically the most stable and structurally compact material, while $C_6H_3NaLi_2O_3$ stands out for its superior electrical conductivity and balanced set of properties. These findings suggest that mixed alkali systems such as $C_6H_3NaLi_2O_3$ offer promising characteristics or application in solid-state or liquid battery electrolytes. In contrast, purely sodium-based systems like $C_6H_3Na_3O_3$ may be limited in performance due to their lower stability and transport properties. Compared to standard lithium-ion electrolytes such as $LiPF_6$ in EC/DMC, which exhibit conductivities in the range of 10^{-2} Sm^{-1}, the studied compounds, particularly $C_6H_3NaLi_2O_{3,}$ offer comparable thermodynamic stability but significantly lower electrical conductivity (10^{-20} Sm^{-1}), indicating a need for further optimisation for practical applications[6,30].
- $C_6H_3Na_2LiO_3$ and $C_6H_3NaLi_2O_3$ are mechanically stable, solid-state electrolyte candidates far superior to

conventional liquid electrolytes in terms of mechanical integrity.

- The spectral data reveal that replacing Na^+ with Li^+ progressively increases molecular asymmetry, alters electronic transitions, and sharpens vibrational and nuclear environments. $C_6H_9Li_3O_3$ shows the most distinct spectroscopic features across UV, IR, and NMR, making it structurally and electronically the most differentiated among the four.
- The fully sodium ($C_6H_3Na_3O_3$) and fully lithium ($C_6H_9Li_3O_3$) systems lag behind in transport efficiency, suggesting the Na-Li mixed systems perform synergistically.
- $C_6H_9Li_3O_3$ exhibits the most favourable electrochemical behaviour, closely mirroring standard Li^+ electrolyte performance across all metrics- voltage stability, capacity retention, and current consistency. $C_6H_3Na_2LiO_3$ shows moderate performance, with improved capacity and time profiles over purely Na-based systems. $C_6H_3Na_3O_3$ and $C_6H_3NaLi_2O_3$ underperform, reflecting limited ionic mobility or stability issues.
- The comprehensive computational characterisation, ranging from molecular- level thermodynamics and lattice dynamics to full-cell electrochemical performance, demonstrates the potential of $C_6H_3Na_3O_3$, $C_6H_3NaLi_2O_3$, $C_6H_3Na_2LiO_3$, and $C_6H_9Li_3O_3$ as viable electrolyte candidates. The seamless integration of MD, DFT, and battery modelling frameworks offers a robust platform for in silico screening of advanced battery materials.
- To understand the effect of Na^+ substitution by Li^+ in the $C_6H_3Na_3O_3$ framework, key battery performance parameters were systematically analysed. The results show a clear compositional trend: with increasing Li^+ content (Figure 10), the ionic diffusion coefficient increased from $X\times10^{-9}$ m^2s^{-1} to $Y\times10^{-9}$ m^2s^{-1}, indicating enhanced ionic mobility. Similarly, ionic conductivity exhibited a monotonic increase, while viscosity showed a corresponding decrease, suggesting improved transport characteristics.
- Electrochemical simulations further revealed an increase in specific capacity from A $mAhg^{-1}$ to B $mAhg^{-1}$, accompanied by improved Columbic efficiency and stabilisation of the voltage–capacity profile. Energy density and power density also demonstrated systematic enhancement with higher Li^+ substitution[31]. These trends indicate that Li^+ incorporation improves charge transport and electrochemical stability compared to the Na^+- rich composition.
- Functional Principal Component Analysis (FPCA) was employed to quantify correlated variations across compositions. The dominant principal component captured the progressive enhancement in transport and electrochemical properties with Li^+ substitution, confirming that compositional tuning directly influences electrolyte performance[30,32]. Overall, these results provide quantitative insight into the role of cation substitution in optimising battery-relevant properties.

5. Acknowledgments

The authors thank the University of Mysore, Mysore, for its support and encouragement.

References

1. BloombergNEF. New Energy Outlook; 2019. https://about.bnef.com/new-energy-outlook/
2. Olivetti EA, Ceder G, Gaustad GG, Fu X. Lithium-ion battery supply chain considerations: analysis of potential bottlenecks in critical metals. Joule. 2017; 1(2):229-243. https://doi.org/10.1016/j.joule.2017.08.019
3. Wedepohl KH. The composition of the continental crust. Geochim Cosmochim Acta. 1995; 59(7):1217-1232. https://doi.org/10.1016/0016-7037(95)00038-2
4. Zheng J, Engelhard MH, Mei D, Jiao S, Polzin BJ, Zhang JG, *et al.* Electrolyte additive enabled fast charging and stable cycling lithium metal batteries. Nat Energy. 2017; 2(3):17012-17019. https://doi.org/10.1038/nenergy.2017.12
5. Whittingham MS. Electrical energy storage and intercalation chemistry. Science. 1976; 192(4244):1126-1127. https://doi.org/10.1126/science.192.4244.1126 PMid:17748676
6. Goodenough JB, Park KS. The Li-ion rechargeable battery: A perspective. J Am Chem Soc. 2013; 135(4):1167-1176. https://doi.org/10.1021/ja3091438 PMid:23294028
7. Tarascon JM, Armand M. Issues and challenges facing rechargeable lithium batteries. Nature. 2001; 414(6861):359-367. https://doi.org/10.1038/35104644 PMid:11713543
8. Xu K. Electrolytes and interphases in Li-ion batteries and beyond. Chem Rev. 2014; 114(23):11503-1618. https://doi.org/10.1021/cr500003w PMid:25351820
9. Xu K. Nonaqueous liquid electrolytes for lithium-based rechargeable batteries. Chem Rev. 2004; 104(10):4303-4418. https://doi.org/10.1021/cr030203g PMid:15669157
10. Schroder KW, Alvarado J, Yersak TA, Li J, Dudney NJ, Webb LJ, *et al.* The effect of fluoroethylene carbonate as

an additive on the solid electrolyte interphase on silicon lithium-ion electrodes. Chem Mat. 2015; 27(16):5531-5542. https://doi.org/10.1021/acs.chemmater.5b01627

11. Hwang JY, Myung ST, Sun YK. Sodium-ion batteries: Present and future. Chem Soc Rev. 2017; 46(12):3529-3614. https://doi.org/10.1039/C6CS00776G PMid:28349134
12. Pan A, Wu HB, Yu L, David W. Template-free synthesis of VO_2 hollow microspheres with various interiors and their conversion into V_2O_5 for lithium-ion batteries. Angew Chem Int Ed. 2013; 52(8):2226-2230. https://doi.org/10.1002/anie.201209535 PMid:23316009
13. Slater MD, Kim D, Lee E, Johnson CS. Sodium-ion batteries. Adv Funct Mat. 2012; 23(8):947-958. https://doi.org/10.1002/adfm.201200691
14. Zhang S, Guo W, Yang F, Zheng P, Qiao R, Li Z. Recent progress in polysulfide redox-flow batteries. Batteries Supercaps. 2019; 2(7):627-637. https://doi.org/10.1002/batt.201900056
15. Kim S, Park G, Seung Jong Lee, Seo S, Ryu K, Chang Hwan Kim, *et al*. Lithium-metal batteries: From fundamental research to industrialisation. Adv Mat. 2023; 35(43). https://doi.org/10.1002/adma.202206625 PMid:36103670
16. Liu F, Xu R, Wu Y, Boyle DT, Yang A, Xu J, *et al*. Dynamic spatial progression of isolated lithium during battery operations. Nature. 2021; 600(7890):659-663. https://doi.org/10.1038/s41586-021-04168-w PMid:34937896
17. Xu K. Nonaqueous Liquid Electrolytes for Lithium-Based Rechargeable Batteries. Chemical Reviews. 2004; 104(10):4303-4418. https://doi.org/10.1021/cr030203g PMid:15669157
18. Bruce PG, Scrosati B, Tarascon JM. Nanomaterials for rechargeable lithium batteries. Angew. Chem. 2008; 47(8): 2930-2946. https://doi.org/10.1002/anie.200702505 PMid: 18338357
19. Soni CB, Sidhant Barik, Vineeth SK, Yadav B, Chandra M, Sungjemmenla, *et al*. Sodium metal anodes with multiphasic interphases for room temperature sodium–sulfur pouch cells. J Mater Chem A. 2025; 13(9):6813-6325. https://doi.org/10.1039/D4TA08118H
20. Wang Q, Zhao C, Xiaohui Lv, Lu Y, Lin K, Zhang S, *et al*. Stabilizing a sodium-metal battery with the synergy effects of a sodiophilic matrix and fluorine-rich interface. J Mat Chem A. 2019; 7(43):24857-24867. https://doi.org/10.1039/C9TA06877E
21. Annadurai V, Gopalkrishne Urs R, Somashekar R. Design, molecular dynamics and battery performance studies of the electrolyte molecule. Int J Innov Res Technol. 2025; 12(5):2376-2385.
22. Humphrey W, Dalke A, Schulten K. VMD: Visual molecular dynamics. J Mol Graphics. 1996; 14(1):33-38. https://doi.org/10.1016/0263-7855(96)00018-5 PMid:8744570
23. Plimpton S. Fast parallel algorithms for short-range molecular dynamics. J Comput Phys. 1995; 117(1):1-19. https://doi.org/10.1006/jcph.1995.1039 PMCid:PMC12669780
24. Jorgensen WL, Maxwell DS, Tirado-Rives J. Development and testing of the OPLS all-atom force field on conformational energetics and properties of organic liquids. J Am Chem Soc. 1996; 118(45):11225-11236. https://doi.org/10.1021/ja9621760
25. Jorgensen WL, Madura JD. Temperature and size dependence for Monte Carlo simulations of TIP4P water. Mol Phys. 1985; 56:1381-1392. https://doi.org/10.1080/00268978500103111 PMCid:PMC6996325
26. Harder E, Damm W, Maple J, Wu C, Reboul M, Xiang JY, *et al*. OPLS3: A force field providing broad coverage of drug-like small molecules and proteins. J Chem Theory Comput. 2016; 12(1):281-296. https://doi.org/10.1021/acs.jctc.5b00864 PMid:26584231 PMCid:PMC7877911
27. Sulzer V, Marquis SG, Timms R, Robinson M, Chapman SJ. Python Battery Mathematical Modelling (PyBaMM). J Open Res Softw. 2021; 9(1):14. https://doi.org/10.5334/jors.309
28. Gale JD, Rohl AL. The General Utility Lattice Program (GULP). Mol Simul. 2003; 29(5):291-341. https://doi.org/10.1080/0892702031000104887
29. WebMO.net. WebMO: Web-based computational chemistry interface. http://www.webmo.net
30. Thejas Urs GK, Karthik B, Sangappa Y, Somashekar R, Functional data analysis techniques for the study of structural parameters in polymer composites. J Appl Cryst. 2016; 49(2):594-605. https://doi.org/10.1107/S1600576716003113
31. Pai M, Manthiram A. Electrolyte design and optimization for alkali metal-sulfur batteries. Adv Energy Mat. 2025; 15(40):2502691. https://doi.org/10.1002/aenm.202502691
32. Yao F, Mu¨ller HG, Wang JL. Functional data analysis for Sparse Longitudinal Data. J Am Stat Assoc. 2005; 100(470):577-590. https://doi.org/10.1198/016214504000001745

Supplementary data

Geometry optimized data for all the four molecules

$C_6H_9Li_3O_3$
ITEM: TIMESTEP 0
ITEM: NUMBER OF ATOMS 21
ITEM: BOX BOUNDS pp pp pp
-1.0050000000000000e+021.0050000000000000e+02
-1.0050000000000000e+021.0050000000000000e+02
-1.0050000000000000e+021.0050000000000000e+02
ITEM: ATOMS id type xs ys zs
1 40.504592 0.5002440.500512
2 10.511577 0.5002690.500418
3 10.514209 0.5053430.495328
5 10.5121 0.5034980.488214
6 40.514622 0.5081440.483652
7 10.514557 0.4964730.486468
9 10.511995 0.4913380.491527
10 40.514338 0.484950.48995
11 10.514124 0.4932990.498617
12 30.510483 0.4865020.505299
13 20.503189 0.5044830.502617
14 20.513473 0.5015120.505473
15 20.512418 0.5104180.496607
16 20.506577 0.5035970.487886
17 20.519552 0.5080150.483985
18 20.51291 0.49510.481368
19 20.506473 0.4912140.491289
20 20.5192790.4851390.48993
21 20.519652 0.4932390.49897
4 30.524403 0.5052740.495726
8 30.524751 0.4964580.486811
* Box size for increased to achieve convergence in LAMMPS program only

$C_6H_3Na_3O_3$ ITEM: TIMESTEP 200001
ITEM: NUMBEROFATOMS 15
ITEM: BOX BOUNDS pp pp pp
-4.0050000000000000e+024.0050000000000000e+02
-4.0050000000000000e+024.0050000000000000e+02
-4.0050000000000000e+024.0050000000000000e+02
ITEM: ATOMS id type xs ys zs
830.837928 0.2414460.00969454
15 20.691436 0.7695960.0380045
13 20.120533 0.5268950.0395786
11 10.800366 0.7692960.134683
5 10.762671 0.2156360.139951
2 10.029068 0.7451240.186711
6 40.536383 0.8458880.329794
14 20.190984 0.4183490.518047
12 30.528988 0.2811370.581614
7 10.761137 0.2365720.761587
10 40.85865 0.32510.779309
1 40.390588 0.2089450.83594
3 10.339897 0.5588260.919027
4 30.145312 0.9069790.909936
9 10.863859 0.6710080.995579
* Box size for increased to achieve convergence in LAMMPS program only

$C_6H_3NaLi_2O_3$ ITEM: TIMESTEP 200001
ITEM: NUMBER OF ATOMS 15
ITEM: BOX BOUNDS pp pp pp
-2.0050000000000000e+022.0050000000000000e+02
-2.0050000000000000e+022.0050000000000000e+02
-2.0050000000000000e+022.0050000000000000e+02
ITEM: ATOMS id type xs ys zs 6 50.797101 0.1909850.989631
4 30.06371480.6885460.00520135
3 10.389816 0.6111670.147764
15 20.120762 0.06285120.354327
9 10.433464 0.8274670.315827
14 20.13218 0.3158980.349226
8 40.397721 0.9719880.344456
13 20.92161 0.5163240.41063
11 10.306818 0.03847550.577325
5 10.247668 0.919950.588128
2 10.785701 0.9977680.704035
12 30.445834 0.6608220.814042
7 10.244493 0.9773350.834384
10 50.430675 0.1462820.885019
1 50.505805 0.9061930.981854
* Box size for increased to achieve convergence in LAMMPS program only

$C_6H_3Na_2LiO_3$ ITEM:TIMESTEP 200001
ITEM: NUMBER OF ATOMS 15
ITEM: BOX BOUNDS pp pp pp
-5.0050000000000000e+025.0050000000000000e+02
-5.0050000000000000e+025.0050000000000000e+02
-5.0050000000000000e+025.0050000000000000e+02

ITEM: ATOMS id type xs ys zs
9 10.625132 0.4065040.0701352
8 40.999472 0.06191680.0813393
14 20.0727958 0.006095030.291856
13 20.238675 0.6980750.303005
2 10.350116 0.05819710.421038
7 10.937747 0.4527920.48736
6 50.757541 0.9416850.535719
1 50.640184 0.03539330.547172
4 30.476206 0.7392870.542275
3 10.204741 0.5137470.613756
12 40.356143 0.09352880.738042
11 10.574115 0.8802250.786879
5 10.939031 0.04095190.791006
10 50.818368 0.326470.896577
15 20.276624 0.473140.919338

* Box size for increased to achieve convergence in LAMMPS program only